

Bidirectional Modulation of HIF-2 Activity through Chemical Ligands

Dalei Wu^{1,2*}, Xiaoyu Su², Jingping Lu², Sheng Li³, Becky L. Hood⁴, Stefan Vasile⁴, Nalini Potluri², Xiaotong Diao¹, Youngchang Kim⁵, Sepideh Khorasanizadeh^{2,6}, Fraydoon Rastinejad^{2,6*}

¹Helmholtz International Lab, State Key Laboratory of Microbial Technology, Shandong University, Qingdao, China.

²Integrative Metabolism Program, Sanford Burnham Prebys Medical Discovery Institute, Orlando, Florida, USA.

³Department of Medicine and UCSD DXMS Proteomics Resource, University of California, San Diego, La Jolla, California, USA.

⁴Conrad Prebys Center for Chemical Genomics, Sanford Burnham Prebys Medical Discovery Institute, Orlando, Florida, USA.

⁵Structural Biology Center, Biosciences Division, Argonne National Laboratory, Argonne, Illinois, USA.

⁶Target Discovery Institute, Nuffield Department of Medicine, University of Oxford, Oxford, UK

*e-mail: fraydoon.rastinejad@ndm.ox.ac.uk or dlwu@sdu.edu.cn

18 **ABSTRACT**

19 **Hypoxia-inducible factor-2 (HIF-2) is a heterodimeric transcription factor formed through**
20 **dimerization between an oxygen-sensitive subunit HIF-2 α subunit and its obligate partner subunit**
21 **ARNT. Enhanced HIF-2 activity drives some cancers, while reduced activity causes anemia in chronic**
22 **kidney disease. Therefore, modulation of HIF-2 activity via direct-binding ligands could provide**
23 **many new therapeutic benefits. Here, we explored HIF-2 α chemical ligands using combined**
24 **crystallographic, biophysical, and cell-based functional studies. We found chemically unrelated**
25 **antagonists to employ the same mechanism of action. Their binding displaced residue M252 from**
26 **inside the HIF-2 α PAS-B pocket toward the ARNT subunit to weaken heterodimerization. We also**
27 **identified first-in-class HIF-2 α agonists and found they significantly displaced pocket residue Y281. Its**
28 **dramatic side-chain movement increases heterodimerization stability and transcriptional activity.**
29 **Our findings show that despite binding to the same HIF-2 α PAS-B pocket, ligands can manifest as**
30 **inhibitors *versus* activators by mobilizing different pocket residues to allosterically alter HIF-2 α -ARNT**
31 **heterodimerization.**

32 **INTRODUCTION**

33 The basic helix-loop-helix-PER-ARNT-SIM (bHLH-PAS) family requires subunit dimerization between its
34 members to form productive transcription factors. A common architectural feature of this family is
35 their highly conserved DNA-binding domain, which must converge symmetrically through subunit
36 dimerization to form a functional DNA-reading head¹. Further unifying the family are their tandem PER-
37 ARNT-SIM (PAS) domains (PAS-A and PAS-B). PAS domains in unrelated protein classes can function as
38 molecular sensors, by binding to environmental and/or physiological ligands². The PAS domains of

39 mammalian bHLH-PAS members not only participate in heterodimer formation¹, but also harbor
40 unique pockets of various size³.

41 The hypoxia-inducible factors (HIFs) within the bHLH-PAS family function as sensors of low oxygen
42 stress, and respond to hypoxia by coordinating genomic pathways in erythropoiesis, angiogenesis and
43 cellular metabolism^{4,5}. The HIF proteins function as obligate heterodimers consisting of one α subunit
44 (any of HIF-1 α , HIF-2 α and HIF-3 α)^{6,7}, and a constitutively-expressed partner β subunit also known as
45 ARNT (aryl hydrocarbon receptor nuclear translocator)⁴. The dimerization of HIF- α and ARNT results in
46 an asymmetric quaternary architecture, creating a DNA-reading head for binding to hypoxia response
47 elements⁸.

48 Molecular oxygen regulates the stability of HIF- α proteins through post-translational
49 modifications. Under normoxia, prolyl hydroxylase domain (PHD) enzymes modify specific proline
50 residues within HIF-1 α and HIF-2 α proteins⁹⁻¹¹, leading to their subsequent proteasomal degradation.
51 An asparagine residue in HIF- α is also targeted by factor inhibiting HIF (FIH) enzyme for hydroxylation
52 under normoxia, further reducing its transcriptional activity^{12,13}. Both of these oxygen-dependent
53 mechanisms suppress HIF activities under normoxia, and are reversed under hypoxia to allow HIF- α
54 protein accumulation and sustained activity.

55 Traditionally, transcription factors were considered difficult drug targets compared to enzymes,
56 kinases, and G-protein coupled receptors. The nuclear receptor (NR) family has been a notable
57 exception due to its conserved ligand-binding domains¹⁴. In the bHLH-PAS family, aryl hydrocarbon
58 receptor (AHR) is known to bind diverse ligands^{15,16}. A select few bHLH-PAS proteins were previously
59 explored for ligand binding within their PAS-B domains, including HIF-2 α ^{17,18}, HIF-1 α ¹⁹, ARNT²⁰ and HIF-

60 3 α ²¹. Based on systematic crystallographic and sequence comparisons, we previously suggested that
61 their entire family harbors cavities for chemical ligands³. Accordingly, new studies are now needed to
62 both identify specific ligands and to examine their functional consequences.

63 The HIF- α proteins serve as an excellent focal point in this regard, due to the recent
64 characterizations of their multi-domain structures⁸. The PT2385 class of HIF-2 α antagonists was
65 recently developed and employed in animal clear cell renal cell carcinoma (ccRCC) tumorgraft models
66 with promising results²²⁻²⁵. However, HIF- α small-molecule agonists have not been previously
67 identified. Such ligands could prove desirable for anemia in the setting of chronic kidney disease
68 (CKD). Currently, PHD enzyme inhibitors are undergoing clinical testing for anemia, as they upregulate
69 HIF-2 activity²⁶⁻²⁸. Direct-binding HIF-2 α agonists could provide advantages or complement the use of
70 PHD inhibitors in CKD anemia, given that both approaches would enhance the expression of the target
71 gene *EPO*²⁹.

72 Here, we examined the ligand-binding capabilities of HIF-2 α -ARNT using distinct chemical ligands,
73 assessing their binding locations and functional manifestations. Relying on new co-crystal structures,
74 hydrogen-deuterium exchange mass spectrometry (H/D-ex MS) data, time-resolved protein binding
75 assays, and functional profiling of target gene expression, we identified allosteric mechanisms by which
76 ligands can produce opposing activities, despite binding to a common binding site within the HIF-2 α
77 protein.

78 **RESULTS**

79 **Biochemical and cellular activities of antagonist PT2385**

80 To assess the antagonistic properties of PT2385 (designated as compound **1** in this study) on HIF-2, we
81 employed complementary biochemical and cell-based assays (**Fig. 1**). Using the recombinant PAS-B
82 domain of HIF-2 α , we found that PT2385 (**Fig. 1a**) binds with an equilibrium binding constant (K_d) of
83 167 nM, as measured by the MST (microscale thermophoresis) method³⁰ (**Fig. 1b**). This affinity was
84 slightly weaker than previously reported K_d of 50 nM measured by ITC (isothermal titration
85 calorimetry)²³, and the difference may be caused by variations in the protein constructs used, assay
86 buffers, or methodologies (ITC vs. MST). Using a FP (fluorescence polarization) assay, we examined if
87 PT2385 changes the binding affinity of HIF-2 α -ARNT heterodimer for its hypoxia response element
88 (HRE) (**Supplementary Fig. 1a**). In the presence of 0 μ M, 0.1 μ M, 1 μ M and 10 μ M PT2385, the DNA
89 binding affinities were 65 nM, 96 nM, 118 nM and 339 nM, respectively, showing a dose-dependent
90 inhibition. However, even at high and saturating concentrations of PT2385, DNA binding was not
91 completely abolished.

92 Using a 786-O cell line stably transfected with the HRE luciferase reporter, we measured an IC₅₀
93 value of 42 nM for PT2385's inhibition of transcriptional activity (**Fig. 1c**). A qPCR assay monitoring the
94 expression of endogenous target genes of HIF-2 (e.g. *VEGF*, *CyclinD1*, *GLUT1* and *NDRG1*) further
95 revealed PT2385's dose-dependent inhibitory activity in 786-O cells (**Fig. 1d**). Recent work
96 demonstrated that PT2385 is selective for HIF-2 α over HIF-1 α , for binding and inhibition of
97 transcriptional activity²³. We previously showed that three residues differed between the PAS-B
98 pockets of HIF-2 α and HIF-1 α , allowing chemical ligands to be highly selective for HIF-2 α *versus* HIF-
99 1 α ⁸. Therefore, it was not surprising that in Hep3B cells, PT2385 decreased the expression of HIF-2
100 specific genes (*VEGF*, *EPO* and *NDRG1*) but not the HIF-1 specific gene (*PGK1*) under hypoxia condition
101 (**Supplementary Fig. 1b**).

102 **Structural and allosteric effects of PT2385**

103 To decipher how PT2385 physically binds to HIF-2 α -ARNT to manifest its actions, we sought the ligand-
104 bound complex structure. The co-crystallization of heterodimer and PT2385 was not successful, but the
105 soaking method allowed us to obtain their complex structure at 3.0 Å resolution (**Supplementary Table**
106 **1**). The PT2385 binding location was unambiguously visualized within the PAS-B pocket of HIF-2 α ,
107 based on “omit” electron density maps (**Fig. 2a, b**). PT2385 contacts multiple HIF-2 α residues inside
108 this pocket, and is stabilized through numerous hydrophobic interactions and a hydrogen bond formed
109 between its hydroxyl group and the H293 side-chain nitrogen (**Fig. 2c**).

110 To learn how PT2385 binding triggers the destabilization of HIF-2 α -ARNT heterodimers, we
111 compared this crystal structure to our previously reported *apo* HIF-2 α -ARNT structure⁸ (**Fig. 2d**). We
112 found a majority of HIF-2 α residues within the pocket undergo only subtle conformational changes
113 upon PT2385 binding, but dramatic changes occur in the positioning of H293 and M252
114 (**Supplementary Fig. 2**). The imidazole ring of H293 turns nearly 45° to form a hydrogen bond with
115 PT2385. Ligand binding further causes a dramatic displacement of the M252 side-chain, forcing it
116 outside the pocket (**Fig. 2d**). The M252 side-chain moves toward a heterodimeric junction between the
117 PAS-B domain of HIF-2 α and the PAS-B domain of ARNT. We previously showed that mutations
118 introduced at this interface destabilize the HIF-2 α -ARNT heterodimer⁸. Therefore, the repositioning of
119 M252 to this junction could account for why PT2385 induces heterodimer destabilization²³.

120 **Effect of PT2385 on heterodimer stability in solution**

121 Because our HIF-2 α -ARNT-PT2385 structure was obtained by soaking instead of co-crystallization, we
122 were concerned that our assessments of PT2385-induced changes could be limited. Therefore, we

123 applied solution-based methods to further probe how PT2385 acts on the heterodimer. We used H/D-
124 ex MS to initially characterize the dynamic features of HIF-2 α -ARNT complex without any bound
125 ligands (**Supplementary Fig. 3a**). The regions with high H/D exchange rates (indicating more flexible
126 backbone structures), were largely located at the polypeptide termini and on loops connecting certain
127 secondary structures within each domain (**Supplementary Fig. 3b**).

128 We then observed changes that PT2385 induced on HIF-2 α -ARNT, by examining the differences in
129 the deuterium exchange patterns of this complex in the presence *versus* the absence of PT2385
130 (**Supplementary Fig. 4**). PT2385 binding dramatically increased the exchange rates of several key
131 regions located in both HIF-2 α and ARNT, suggesting an allosteric effect in which protein regions distal
132 to the ligand-binding site are impacted (**Fig. 2d**). By mapping these altered regions onto our crystal
133 structure of HIF-2 α -ARNT, we found changes are induced at domain-domain interfaces responsible for
134 maintaining heterodimer stability (**Fig. 2e**).

135 Not surprisingly, the HI loop (located between H β and I β) of ARNT PAS-B domain interacting with
136 HIF-2 α PAS-B, which we had observed to be pushed away due to the PT2385-induced movement of
137 M252 (**Fig. 2d**, right), displayed increased H/D exchange and enhanced dynamics upon PT2385 binding
138 (**Fig. 2e**, left). The C-terminus of HIF-2 α PAS-B domain, which contributes to the same PAS-B/PAS-B
139 interface, also showed enhanced exchange, suggesting destabilization (**Fig. 2e**, left). Several α -helices
140 mediating interactions between bHLH and PAS-A domains of both HIF-2 α and ARNT, were also
141 destabilized, as inferred from their higher exchange rates, suggesting even more distal effects by
142 PT2385 (**Fig. 2e**, right).

143 These H/D-ex MS observations vividly illustrate how binding of PT2385 to the HIF-2 α PAS-B
144 domain impacts multiple domain interfaces simultaneously, all at a considerable distance to its physical

145 binding pocket, extending as far away as the bHLH DNA reading head of the complex. Since the latter
146 allosteric effects are less pronounced, they help explain why the DNA-binding affinity of the
147 heterodimer are not completely eliminated (**Supplementary Fig. 1a**).

148 **Effect of PT2385 on the affinity between HIF-2 α and ARNT**

149 We next sought to measure the binding affinity between HIF-2 α and ARNT proteins in forming their
150 heterodimer. As PT2385 dose-dependently reduced their interactions in cells (**Fig. 3a**), we assessed
151 whether the complete or partial dissociation of the heterodimer would result with PT2385 addition *in*
152 *vitro*. We developed a TR-FRET-based binding assay that could detect interactions between the two
153 subunits (**Supplementary Fig. 5a**). Because the K_d values for ARNT and any of its heterodimerization
154 partners were not previously determined, we first measured these equilibrium affinity constants of
155 ARNT with a variety of known dimerization partners within the bHLH-PAS family, including HIF-2 α , HIF-
156 1 α and NPAS3 (neuronal PAS domain protein 3).

157 The apparent K_d values that we detected for ARNT binding to each of HIF-2 α , HIF-1 α and NPAS3,
158 were 29.1 nM, 11.7 nM and 8.6 nM, respectively (**Supplementary Fig. 5b-d**). An important caveat to
159 consider is the single nM-level affinity between the anti-His antibody and the His-tag protein subunit
160 employed in this assay. Therefore, we may have been limited in detecting the actual K_d values if the
161 true binding affinities are below the 10 nM level. Still, this assay provides an excellent means to
162 monitor changes in affinity caused by ligand binding, or by point mutations on each protein.

163 We then used this assay to ask how PT2385 alters the dimerization affinities in each of HIF-2 α -
164 ARNT and HIF-1 α -ARNT complexes (**Fig. 3b,c**). Ligand binding disrupted the dimerization between HIF-
165 2 α and ARNT with a K_i of 148 nM (**Fig. 3b**). However, the disruption of the subunits did not appear

complete, as the TR-FRET value only changed 50%. This observation could be interpreted in two ways: either half of the complexes are fully dissociated and the remaining half are unaffected, or 100% of heterodimers undergo a partial separation of subunits. However, only the latter interpretation is consistent with our other solution-based studies. The H/D-ex MS data is inconsistent with the notion that the subunits actually dissociate completely into non-interacting monomers (i.e., we did not observe substantial increases in H/D patterns throughout the outside surfaces of both subunits). Moreover, we noted partial retention of DNA-binding activity even under saturating concentrations of PT2385, again inconsistent with full separation of the two subunits. Importantly, our TR-FRET studies detected no PT2385 effect on HIF-1 α -ARNT subunit interactions (**Fig. 3c**), consistent with its HIF-2 α selectivity.

Exploring PT2385's allosteric mechanism by mutagenesis

As described above, our crystallographic studies suggested that the HIF-2 α pocket residue, M252, mediates the allosteric effects of PT2385 binding to distal sites at the heterodimer junctions (**Fig. 2d**). To fully understand the importance of this residue, we generated a point mutation M252A in HIF-2 α and conducted additional TR-FRET studies (**Fig. 3d,e**). We first detected how this mutation altered the ability of HIF-2 α and ARNT to heterodimerize. The apparent K_d value for the mutant HIF-2 α binding to ARNT was 1.4 nM (**Fig. 3d**), much lower than that of wild-type (WT) HIF-2 α binding to ARNT (29.1 nM). We then examined PT2385's effects on the mutant heterodimer. Compared to the WT HIF-2 α (**Fig. 3b**), the M252A mutant was notably resistant to heterodimer disruption by PT2385 (**Fig. 3e**).

We employed cell-based functional studies to assess the differences in the function of WT and mutant heterodimers. Compared to the activity of WT HIF-2 α transfected HEK293T cells, in which the expression of HIF-2 target genes (i.e. *VEGFA*, *EPO* and *NDRG1*) was substantially reduced by PT2385,

188 the same cells transfected with HIF-2 α mutant M252A showed no significant inhibitory effects by
189 PT2385 (**Fig. 3f**). These functional studies with the M252A mutant, support our crystallographic
190 inference that M252 is critical for mediating PT2385's disruption of heterodimer.

191 In animal studies using the ccRCC tumorgraft model²⁴, two point mutations (HIF-2 α G323E and
192 ARNT F446L) were previously reported to be acquired after prolonged treatment with PT2399 (PT2385
193 analog), causing drug resistance. PT2399 could not disassociate HIF-2 α -ARNT in cells when either
194 mutation was present. G323E locates inside the PAS-B pocket of HIF-2 α , and the large side-chain of a
195 glutamic acid replacement would occlude PT2399's binding, accounting for drug resistance. However,
196 ARNT F446L locates at a heterodimer interface, and its role in resistance to PT2399 was not obvious
197 (**Supplementary Fig. 5e**).

198 To investigate the impact of these two resistance mutations on the association between HIF-2 α
199 and ARNT, we employed our TR-FRET-based assay. HIF-2 α G323E mutation only modestly increased
200 the affinity between two subunits (apparent K_d about 10.5 nM) (**Supplementary Fig. 5f**), but
201 dramatically reduced PT2385's ability to impact heterodimer stability (**Supplementary Fig. 5g**). We
202 interpret these data as consistent with our structural finding that this mutation restricts PT2385's
203 access to its pocket.

204 Interestingly, the ARNT F446L mutation substantially enhanced the natural affinity of ARNT for
205 HIF-2 α (apparent K_d about 0.8 nM, compared to 29.1 nM in the WT) (**Supplementary Fig. 5h**),
206 consistent with the positioning of this mutation at a dimer interface where it reinforces junctional
207 stability. At the same time, PT2385 was able to still reduce the heterodimer stability in a dose-
208 dependent manner with this mutation (K_i of 127 nM), consistent with unobstructed access of the drug

209 to its pocket (**Supplementary Fig. 5i**). These data explain previously unknown aspects of *in vivo*
210 resistance due to both mutations²⁴.

211 **Diverse antagonist chemotypes employ the same mechanism**

212 While our data portray the mechanism of action used by PT2385 is allosteric and based on the partial
213 destabilization of the heterodimer, it is unclear whether other small-molecule antagonists would also
214 use this mechanism. We attempted to discover new HIF-2 antagonist chemotypes and to compare
215 their mechanistic basis of action. Using purified HIF-2 α -ARNT complex proteins, we created a high-
216 throughput assay based on protein thermal shift changes³¹ for *in vitro* screening of chemical libraries.
217 One hit that emerged from the LOPAC library was S(-)-*p*-bromotetramisole (designated as compound **2**
218 or T1001, **Fig. 4a**), which increased the protein melting temperature of the complex (T_m) by
219 approximately 1.5 °C (**Supplementary Fig. 6**). T1001 bound to the PAS-B domain of HIF-2 α with a K_d of
220 about 246 nM, as measured by MST (**Fig. 4b**). In studying its cellular effects on the expression of known
221 HIF-2 target genes in 786-O cells (**Fig. 4c**), we found that compared to PT2385, T1001 was a weaker
222 antagonist.

223 We obtained the co-crystal structure of HIF-2 α -ARNT with T1001. The “omit” map in **Fig. 4d** shows
224 that T1001 binds into the same PAS-B domain of HIF-2 α as PT2385 (**Supplementary Fig. 7**). We asked if
225 the HIF-2 α residue M252 was also essential in mediating the inhibitory effects of T1001, and found that
226 the expression of HIF-2 target genes (i.e. *VEGFA* and *EPO*) was suppressed by T1001 in the presence of
227 WT HIF-2 α , but not in the presence of the M252A mutant (**Fig. 4e**). These results confirmed that M252
228 residue is similarly important for T1001’s antagonistic activity.

229 Using H/D-ex MS studies, we found that T1001, like PT2385, produces a modest destabilizing
230 effect at several junctions of the HIF-2 α -ARNT heterodimer (**Supplementary Fig. 8a**). The locations of
231 enhanced deuterium exchange rates on the crystal structure map to domain interfaces where PT2385
232 had also impacted (**Fig. 2e** and **Supplementary Fig. 8b**). Thus, our crystallographic, H/D-ex MS and
233 mutation-based functional assays show a common allosteric mechanism employed by two chemically
234 unrelated antagonists.

235 In addition to these two antagonists, we previously described the binding mode of antagonist
236 OX3^{8,32}. We made further comparisons among HIF-2 α -ARNT crystal structures bound to each of
237 PT2385, T1001 and OX3. These ligands rely on a similar constellation of amino-acid residues for their
238 binding, but their abilities to physically displace M252 from the pocket are notably different (**Fig. 4f**).
239 PT2385 causes the most significant displacement for M252 side-chain, forcing it completely outside of
240 the PAS-B pocket. OX3 has a moderate impact, and T1001 produces the least displacement. The
241 extents of movement by M252 from inside the pocket and toward the dimer interface correlate with
242 the relative potencies of these antagonists (**Fig. 4g**). This key information should guide the future
243 development of new antagonists.

244 **Identification of HIF-2 agonists**

245 We sought first-in-class HIF-2 α binding ligands that could increase the transcriptional activity of HIF-2.
246 Although agonists were not previously identified, the possibility that PAS pockets would allow
247 upregulation of HIF-2 activity was plausible. This is because several cancer-related missense mutations
248 in the pockets of PAS-A or PAS-B domains of HIF-2 α protein^{8,33} increased transcriptional activity
249 (**Supplementary Fig. 9a,b**). Therefore, we reasoned that the pockets were wired to enhance
250 transcriptional activity through their interior contact residues. Interestingly, these cancer mutations

251 did not result in detectable changes in stabilities of HIF-2 α and ARNT heterodimers, based on our Co-IP
252 studies (**Supplementary Fig. 9c**).

253 Our previous protein thermal shift screens had employed small chemical libraries, leading us not
254 to find agonists. Therefore, we took a more efficient approach based on affinity selection-mass
255 spectrometry (AS-MS) screening³⁴ employing a larger chemical library of 32,000 compounds. M1001
256 (designated as compound **3**, **Fig. 5a**) emerged as the only hit with agonistic activity. M1001 binding
257 increased the T_m of HIF-2 α -ARNT complex by 0.8 °C in the thermal shift assay (**Supplementary Fig. 6**),
258 and it was subsequently found to bind to the HIF-2 α PAS-B domain by MST (**Fig. 5b**). 786-O cells
259 treated with M1001 showed modestly increased expression of HIF-2 target genes, producing the
260 opposite response of PT2385 (**Fig. 5c**). These data confirmed that M1001 directly binds to HIF-2 α and
261 has the properties of a weak agonist.

262 **Structure-function studies to reveal agonistic mechanism**

263 We solved the complex structure of the heterodimer bound to M1001, observing the ligand inside the
264 PAS-B domain of HIF-2 α (**Fig. 5d**), as seen in “omit” maps (**Fig. 5e**). Like the antagonists, M1001 binding
265 was stabilized through hydrophobic interactions and a single hydrogen bond with the backbone oxygen
266 of residue A277 (**Fig. 5f**). Most of the residues surrounding M1001 adopt similar conformations as in
267 the *apo* HIF-2 α -ARNT complex, except for Y281 that undergoes a striking displacement
268 (**Supplementary Fig. 10a**). Upon M1001 binding, the side-chain ring of Y281 flips out from inside the
269 HIF-2 α pocket and moves towards the ARNT subunit, creating a new hydrogen bond between HIF-2 α
270 and ARNT through the latter’s Y456 residue (**Fig. 5g**, right). This new contact appears to confer added
271 stability to the heterodimer.

272 In all of our previous structural studies with the unliganded or antagonist-bound forms of the HIF-
273 2 α -ARNT complexes, we had found a loop connecting ARNT PAS-A and PAS-B domains (A/B loop) to be
274 disordered (lacking electron density). However, in the M1001-bound complex, we detected clear
275 electron density for the first time, consistent with a ligand-stabilized ARNT A/B loop (**Supplementary**
276 **Fig. 10b,c**). We could assign nearly all the residues of this loop. Aside from M1001 stabilizing this
277 segment, the F α helix of M1001-bound HIF-2 α PAS-B domain also moved towards the A/B loop (**Fig. 5g**
278 left), further enhancing the subunit interface between HIF-2 α and ARNT A/B loop (now with newly
279 formed contact between E287 from HIF-2 α F α helix and N350 from the A/B loop of ARNT). These
280 observations indicate that M1001's binding to HIF-2 α allosterically enhances the stabilities of protein
281 segments, and enhances the interfacial junctions connections of HIF-2 α and ARNT.

282 To assess if the solution state of the complex was also more stable in the presence of M1001, we
283 employed the H/D-ex MS method to examine the altered dynamics of HIF-2 α -ARNT. In clear
284 opposition to antagonists PT2385 and T1001, M1001 produced a more stabilizing effect on various
285 segments of the HIF-2 α -ARNT complex (**Supplementary Fig. 11**). Closely examining the individual
286 regions undergoing reduced H/D exchange, two critical locations are worth noting (**Fig. 5h**). One region
287 is the PAS-B/PAS-B dimer interface, where the HI loop of ARNT PAS-B and the C-terminus of HIF-2 α
288 PAS-B are stabilized by M1001 binding (**Fig. 5h**, left), in opposition to the actions of antagonists (**Fig. 2e**
289 and **Supplementary Fig. 8b**, both left). The second region is the PAS-A/PAS-B interface within the HIF-
290 2 α subunit, where several secondary structural elements become stabilized, including the second half
291 of F α , G β and H β in PAS-B domain, and the first half of G β in PAS-A domain (**Fig. 5h**, right). These
292 solution-based data confirm that M1001 enhances the stabilities of subunit interactions at multiple
293 locations, in contrast to antagonists.

294 Since agonism by M1001 was modest, we relied on a structure-activity relationship (SAR) approach
295 to search through chemically related M1001 analogs commercially available, and to identify molecules
296 with increased potency and/or efficacy. One analog, M1002 (designated as compound **4**, **Fig. 6a**),
297 increased the T_m value of HIF-2 α -ARNT complex by approximately 1.8 °C in the thermal shift assay
298 (**Supplementary Fig. 6**), substantially more than the 0.8 °C seen with M1001. In 786-O cells, M1002
299 enhanced the expression of HIF-2 target genes with greater efficacy than M1001 (**Fig. 6b** and **Fig. 5c**).

300 To see how the M1001/M1002 agonist class could impact the physical dimerization between
301 isolated HIF-2 α and ARNT proteins in solution, we used the TR-FRET-based assay. As shown in **Fig. 6c**,
302 M1002 enhanced the physical association of HIF-2 α and ARNT in a dose-dependent fashion. To assess
303 its selectivity for HIF-2 α , we studied its effects on both HIF-1 α -ARNT and NPAS3-ARNT complexes.
304 M1002 could increase the interactions between HIF-1 α and ARNT, but only at higher compound
305 concentrations. But M1002 had no discernible effect on the association of NPAS3 with ARNT (**Fig. 6c**).

306 To address the mechanistic question of whether the agonistic effect of M1002 was dependent on
307 HIF-2 α residue Y281 (**Fig. 5g**), we made a point mutation Y281A and compared activities with WT when
308 overexpressing each protein in HEK293T cells. M1002 treatment increased the expression of HIF-2
309 target genes (i.e. *VEGA*, *EPO* and *NDRG1*) with the WT protein, but not with the Y281A mutant (**Fig.**
310 **6d**), pointing to Y281 as a critical element in its allosteric action.

311 As the von Hippel-Lindau (VHL) tumor suppressor protein binds to HIF- α proteins to regulate their
312 stability, we further tested if HIF-2 α ligands might change the extent of interaction between VHL and
313 HIF-2 α . We co-transfected HEK293T cells with plasmids encoding both full-length proteins, and treated
314 cells with different ligands. As shown by the co-IP results in **Fig. 6e**, in contrast to the antagonists

315 (PT2385 and T1001), two agonists (M1001 and M1002) could reduce the physical association between
316 HIF-2 α and VHL. The reduced VHL binding to HIF-2 α in the presence of agonists could be due to the
317 intrinsically weakened interactions between their proteins caused by the conformational changes
318 induced in HIF-2 α , or due to secondary effects the compounds may have in reducing proline
319 hydroxylation levels on HIF-2 α .

320 **Potential synergy of HIF-2 α agonists and PHD inhibitors**

321 The activation of HIF pathways may be clinically desirable in renal anemia and ischemia^{26,35}. Several
322 small-molecule compounds are in clinical trials to treat anemia in CKD patients, notably roxadustat (FG-
323 4592)³⁶, daprodustat (GSK1278863)³⁷, vadadustat (AKB-6548)³⁸ and molidustat (BAY 85-3934)³⁹. All of
324 these are PHD inhibitors which boost HIF-2 α protein levels, leading to increased HIF-2 activity and the
325 production of endogenous EPO²⁹.

326 Since PHD inhibitors activate the HIF-2 pathway indirectly, in contrast to the agonists we described
327 here that bind directly to HIF-2 α , we asked whether the combination of these two types of approaches
328 could synergistically stimulate *EPO* expression. We selected two known PHD inhibitors (molidustat and
329 roxadustat), and examined their effects on the expression of HIF target genes in Hep3B cells co-treated
330 with M1002 (**Supplementary Fig. 12**). The PHD inhibitors increased the expression of HIF-2 target
331 genes (*EPO* and *NDRG1*) about 3-5 fold, but had relatively small effects on HIF-1 selective target gene
332 (*PGK1*). M1002 alone at low concentration produced little enhancement on gene expression.
333 However, co-treatment of this same concentration of M1002 together with PHD inhibitors elevated the
334 expression of *EPO* and *NDRG1* but not that of *PGK1*, suggesting synergy between HIF-2 α agonists and
335 PHD inhibitors.

336 DISCUSSION

337 We investigated the activities, binding sites, and allosteric mechanisms of known and newly discovered
338 HIF-2 modulators, and found all to influence the stability of HIF-2 α -ARNT complex allosterically. By
339 comparing the crystal structures of HIF-2 α -ARNT in complex with various antagonists (including
340 PT2385, T1001 and OX3), we found that ligand-induced movement of HIF-2 α pocket residue M252's
341 side-chain was critical in destabilizing the heterodimeric complex formed between HIF-2 α and ARNT.
342 We further found that the relative potency of the antagonists correlated with the degree to which they
343 could physically displace the M252 side-chain from inside of pocket and point it towards the dimer
344 interface.

345 While PT2385 is a potent inhibitor, the resistance mutations that arise due to its extended
346 exposure *in vivo* could limit its long-term effectiveness and ultimately necessitate the use of new
347 classes of antagonists for prolonged therapy²⁴. In addition to the PAS-B domain binding compounds
348 emphasized here and in prior studies^{32,40-42}, new antagonists that bind to other pockets of HIF-2 α -ARNT
349 complex (e.g. PAS-A domain) could prove equally promising⁸. In this regard, our thorough structural
350 description of this ligand pocket, together with residue M252's allosteric role should facilitate the
351 discovery of many novel and potent antagonists. OX3, PT2385 and T1001 are chemically unrelated to
352 each other, yet all bind effectively with an overlapping footprint to the same pocket. This observation
353 shows the PAS-B domain pocket of HIF-2 α to be highly accommodative for a wide-variety of distinct
354 chemical ligands and ideal for further ligand discovery.

355 In terms of agonists, we showed for the first time that small-molecules capable of activating HIF-
356 2 α protein could be discovered from high-throughput screens. These agonists could provide an
357 alternative approach to treating renal anemia. Some PHD inhibitors are currently in Phase III clinical

358 trials, validating the HIF-2/PHD axis as an effective target for increasing EPO protein levels and
359 ameliorating anemia²⁶⁻²⁸. However, a possible disadvantage of PHD inhibitors may be that their other
360 targets, unrelated to the HIF-2 α protein, could create undesired side-effects during anemia therapy.
361 Direct-binding HIF-2 α agonists should be explored given their likelihood to produce fewer side-effects.
362 The agonist class we discovered here binds to the same HIF-2 α PAS-B pocket as the antagonists.
363 However, we observed agonists trigger the movement of an altogether different residue from inside
364 the pocket, namely Y281. This displaced residue stabilizes the overall conformations and enhances
365 subunit dimerization, in contrast to role of M252 in mediating the effects of antagonists.

366 Our studies here also show for the first time that HIF-2 can be functionally modulated in a
367 bidirectional manner (agonists *versus* antagonists) through chemical ligands, even when these ligands
368 bind to precisely the same PAS-B pocket of HIF-2 α . The gain-of-function cancer related mutations that
369 mapped directly to HIF-2 α pockets foreshadowed the possibility of upregulating functional activity
370 using agonists that contact these pockets. In the future, similar sets of studies with other mammalian
371 bHLH-PAS family members are needed to assess if they too are amenable to activation and inhibition
372 via direct-binding chemical ligands.

373 **Acknowledgements**

374 We thank members of the Structural Biology Center at Argonne National Laboratory for their help with
375 data collection at the 19-ID beamline, and Garib N. Murshudov at University of Cambridge for the help
376 with ligand building at the 2016 CCP4/APS summer school. This work was supported by Welcome
377 Trust, and by grants from the National Institutes of Health (R01GM117013, R01DK118297) and U.S.
378 ARMY Medical Research (W81XWH-16-1-0322) to F.R., as well as grants from Shandong University

379 (Qilu Young Scholar 86963072), National Natural Science Foundation of China (31700114), Natural
380 Science Foundation of Jiangsu Province (BK20170399), and the 111 Project (B16030) to D.W.

381 **Author contributions**

382 D.W. purified proteins, carried out crystallization, and solved the structures. X.S. conducted cell-based
383 experiments. J.L. purified proteins and performed biochemical assays. S.L. executed the H/D-ex MS
384 analysis. B.H. and S.V. performed the TR-FRET binding assays and thermal shift-based screening
385 experiments. N.P. produced the expression and mutation constructs. X.D. contributed to biochemical
386 assays and structure refinement. Y.K. collected and processed synchrotron diffraction data. S.K.
387 provided critical instruments and training for biochemical studies. All authors analyzed results. D.W.
388 and F.R. conceived this study, designed experiments, and wrote the manuscript.

389 **Competing financial interests**

390 The authors declare no competing financial interests.

391 **References**

- 392 1. Wu, D. & Rastinejad, F. Structural characterization of mammalian bHLH-PAS transcription
393 factors. *Curr Opin Struct Biol* **43**, 1-9 (2017).
- 394 2. Moglich, A., Ayers, R.A. & Moffat, K. Structure and signaling mechanism of Per-ARNT-Sim
395 domains. *Structure* **17**, 1282-94 (2009).
- 396 3. Wu, D., Su, X., Potluri, N., Kim, Y. & Rastinejad, F. NPAS1-ARNT and NPAS3-ARNT crystal
397 structures implicate the bHLH-PAS family as multi-ligand binding transcription factors. *Elife* **5**,
398 e18790 (2016).
- 399 4. McIntosh, B.E., Hogenesch, J.B. & Bradfield, C.A. Mammalian Per-Arnt-Sim proteins in
400 environmental adaptation. *Annu Rev Physiol* **72**, 625-45 (2010).
- 401 5. Schito, L. & Semenza, G.L. Hypoxia-Inducible Factors: Master Regulators of Cancer Progression.
402 *Trends Cancer* **2**, 758-770 (2016).

- 403 6. Keith, B., Johnson, R.S. & Simon, M.C. HIF1alpha and HIF2alpha: sibling rivalry in hypoxic
404 tumour growth and progression. *Nat Rev Cancer* **12**, 9-22 (2011).
- 405 7. Ravenna, L., Salvatori, L. & Russo, M.A. HIF3alpha: the little we know. *FEBS J* **283**, 993-1003
406 (2016).
- 407 8. Wu, D., Potluri, N., Lu, J., Kim, Y. & Rastinejad, F. Structural integration in hypoxia-inducible
408 factors. *Nature* **524**, 303-8 (2015).
- 409 9. Ivan, M. et al. HIFalpha targeted for VHL-mediated destruction by proline hydroxylation:
410 implications for O2 sensing. *Science* **292**, 464-8 (2001).
- 411 10. Jaakkola, P. et al. Targeting of HIF-alpha to the von Hippel-Lindau ubiquitylation complex by O2-
412 regulated prolyl hydroxylation. *Science* **292**, 468-72 (2001).
- 413 11. Yu, F., White, S.B., Zhao, Q. & Lee, F.S. HIF-1alpha binding to VHL is regulated by stimulus-
414 sensitive proline hydroxylation. *Proc Natl Acad Sci U S A* **98**, 9630-5 (2001).
- 415 12. Lando, D., Peet, D.J., Whelan, D.A., Gorman, J.J. & Whitelaw, M.L. Asparagine hydroxylation of
416 the HIF transactivation domain a hypoxic switch. *Science* **295**, 858-61 (2002).
- 417 13. Lando, D. et al. FIH-1 is an asparaginyl hydroxylase enzyme that regulates the transcriptional
418 activity of hypoxia-inducible factor. *Genes Dev* **16**, 1466-71 (2002).
- 419 14. Huang, P., Chandra, V. & Rastinejad, F. Structural overview of the nuclear receptor superfamily:
420 insights into physiology and therapeutics. *Annu Rev Physiol* **72**, 247-72 (2010).
- 421 15. Denison, M.S. & Nagy, S.R. Activation of the aryl hydrocarbon receptor by structurally diverse
422 exogenous and endogenous chemicals. *Annu Rev Pharmacol Toxicol* **43**, 309-34 (2003).
- 423 16. Denison, M.S., Soshilov, A.A., He, G., DeGroot, D.E. & Zhao, B. Exactly the same but different:
424 promiscuity and diversity in the molecular mechanisms of action of the aryl hydrocarbon
425 (dioxin) receptor. *Toxicol Sci* **124**, 1-22 (2011).
- 426 17. Scheuermann, T.H. et al. Artificial ligand binding within the HIF2alpha PAS-B domain of the HIF2
427 transcription factor. *Proc Natl Acad Sci U S A* **106**, 450-5 (2009).
- 428 18. Key, J., Scheuermann, T.H., Anderson, P.C., Daggett, V. & Gardner, K.H. Principles of ligand
429 binding within a completely buried cavity in HIF2alpha PAS-B. *J Am Chem Soc* **131**, 17647-54
430 (2009).

- 431 19. Cardoso, R. et al. Identification of Cys255 in HIF-1alpha as a novel site for development of
432 covalent inhibitors of HIF-1alpha/ARNT PasB domain protein-protein interaction. *Protein Sci* **21**,
433 1885-96 (2012).
- 434 20. Guo, Y. et al. Regulating the ARNT/TACC3 axis: multiple approaches to manipulating
435 protein/protein interactions with small molecules. *ACS Chem Biol* **8**, 626-35 (2013).
- 436 21. Fala, A.M. et al. Unsaturated fatty acids as high-affinity ligands of the C-terminal Per-ARNT-Sim
437 domain from the Hypoxia-inducible factor 3alpha. *Sci Rep* **5**, 12698 (2015).
- 438 22. Hewitson, K.S. & Schofield, C.J. The HIF pathway as a therapeutic target. *Drug Discov Today* **9**,
439 704-11 (2004).
- 440 23. Wallace, E.M. et al. A Small-Molecule Antagonist of HIF2alpha Is Efficacious in Preclinical
441 Models of Renal Cell Carcinoma. *Cancer Res* **76**, 5491-500 (2016).
- 442 24. Chen, W. et al. Targeting renal cell carcinoma with a HIF-2 antagonist. *Nature* **539**, 112-117
443 (2016).
- 444 25. Cho, H. et al. On-target efficacy of a HIF-2alpha antagonist in preclinical kidney cancer models.
445 *Nature* **539**, 107-111 (2016).
- 446 26. Maxwell, P.H. & Eckardt, K.U. HIF prolyl hydroxylase inhibitors for the treatment of renal
447 anaemia and beyond. *Nat Rev Nephrol* **12**, 157-68 (2016).
- 448 27. Yousaf, F. & Spinowitz, B. Hypoxia-Inducible Factor Stabilizers: a New Avenue for Reducing BP
449 While Helping Hemoglobin? *Curr Hypertens Rep* **18**, 23 (2016).
- 450 28. Gupta, N. & Wish, J.B. Hypoxia-Inducible Factor Prolyl Hydroxylase Inhibitors: A Potential New
451 Treatment for Anemia in Patients With CKD. *Am J Kidney Dis* **69**, 815-826 (2017).
- 452 29. Yeh, T.L. et al. Molecular and cellular mechanisms of HIF prolyl hydroxylase inhibitors in clinical
453 trials. *Chem Sci* **8**, 7651-7668 (2017).
- 454 30. Seidel, S.A. et al. Microscale thermophoresis quantifies biomolecular interactions under
455 previously challenging conditions. *Methods* **59**, 301-15 (2013).
- 456 31. Ciulli, A. & Abell, C. Fragment-based approaches to enzyme inhibition. *Curr Opin Biotechnol* **18**,
457 489-96 (2007).
- 458 32. Scheuermann, T.H. et al. Allosteric inhibition of hypoxia inducible factor-2 with small molecules.
459 *Nat Chem Biol* **9**, 271-6 (2013).

- 460 33. Forbes, S.A. et al. COSMIC: exploring the world's knowledge of somatic mutations in human
461 cancer. *Nucleic Acids Res* **43**, D805-11 (2015).
- 462 34. Annis, D.A., Nickbarg, E., Yang, X., Ziebell, M.R. & Whitehurst, C.E. Affinity selection-mass
463 spectrometry screening techniques for small molecule drug discovery. *Curr Opin Chem Biol* **11**,
464 518-26 (2007).
- 465 35. Bonomini, M., Del Vecchio, L., Sirolli, V. & Locatelli, F. New Treatment Approaches for the
466 Anemia of CKD. *Am J Kidney Dis* **67**, 133-42 (2016).
- 467 36. Besarab, A. et al. Roxadustat (FG-4592): Correction of Anemia in Incident Dialysis Patients. *J Am*
468 *Soc Nephrol* **27**, 1225-33 (2016).
- 469 37. Brigandi, R.A. et al. A Novel Hypoxia-Inducible Factor-Prolyl Hydroxylase Inhibitor (GSK1278863)
470 for Anemia in CKD: A 28-Day, Phase 2A Randomized Trial. *Am J Kidney Dis* **67**, 861-71 (2016).
- 471 38. Pergola, P.E., Spinowitz, B.S., Hartman, C.S., Maroni, B.J. & Haase, V.H. Vadadustat, a novel oral
472 HIF stabilizer, provides effective anemia treatment in nondialysis-dependent chronic kidney
473 disease. *Kidney Int* **90**, 1115-1122 (2016).
- 474 39. Beck, H. et al. Discovery of Molidustat (BAY 85-3934): A Small-Molecule Oral HIF-Prolyl
475 Hydroxylase (HIF-PH) Inhibitor for the Treatment of Renal Anemia. *ChemMedChem* **13**, 988-
476 1003 (2018).
- 477 40. Rogers, J.L. et al. Development of inhibitors of the PAS-B domain of the HIF-2alpha transcription
478 factor. *J Med Chem* **56**, 1739-47 (2013).
- 479 41. Scheuermann, T.H. et al. Isoform-Selective and Stereoselective Inhibition of Hypoxia Inducible
480 Factor-2. *J Med Chem* **58**, 5930-41 (2015).
- 481 42. Wehn, P.M. et al. Design and Activity of Specific Hypoxia-Inducible Factor-2alpha (HIF-2alpha)
482 Inhibitors for the Treatment of Clear Cell Renal Cell Carcinoma: Discovery of Clinical Candidate
483 (S)-3-((2,2-Difluoro-1-hydroxy-7-(methylsulfonyl)-2,3-dihydro-1 H-inden-4-yl)oxy)-5-
484 fluorobenzonitrile (PT2385). *J Med Chem* (2018).
- 485

486 **Figure Legends**

487 **Figure 1 Inhibition of HIF-2 by PT2385.** **a**, Chemical structure of PT2385. **b**, Binding of PT2385 to the
488 HIF-2 α PAS-B domain (K_d about 167 nM) as measured by MST. **c**, Dose-dependent inhibition of HRE
489 luciferase reporter activity by PT2385. **d**, Expression of HIF-2 target genes in 786-O cells after
490 treatment with PT2385 at various concentrations (0.01, 0.1, 1 or 10 μ M). Error bars, mean \pm s.d.; n=3
491 (distinct replicates for cell cultures).

492 **Figure 2 Allosteric mechanism of PT2385 revealed by the crystal structure and H/D-ex MS.** **a**, Binding
493 position for PT2385 (circled in black) within the entire HIF-2 α -ARNT crystal structure. **b**, Close-up look
494 at the location of PT2385 inside the HIF-2 α PAS-B domain, with green mesh showing the $F_o - F_c$ omit
495 map contoured at 2.7σ . **c**, Interactions of PT2385 (yellow) with surrounding residues in the pocket. **d**,
496 The overall arrangement of ARNT and HIF-2 α PAS-B domains is displayed on the left, with the HIF-2 α
497 PAS-B from PT2385-bound (magenta) or *apo* (orange) complexes superimposed. On the right, an
498 enlarged and rotated view shows the different side-chain orientations of M252 in these two
499 complexes. The side-chain movement of HIF-2 α M252 caused by antagonist binding disrupts the
500 dimerization of HIF-2 α -ARNT complex at the PAS-B/PAS-B interface. **e**, H/D-ex MS results mapped on
501 the crystal structure of HIF-2 α -ARNT complex. The regions showing dynamic changes upon PT2385
502 binding are colored according to the maximum differences of deuteration levels (red for 40 to 50%,
503 pink for 25 to 40%) as compared to the *apo* form complex (detailed in **Supplementary Fig. 4**), on top of
504 the background colors of HIF-2 α (gray) and ARNT (pale yellow). Enlarged and rotated views of dimer
505 interfaces between the PAS-B domains, and among the PAS-A and bHLH domains are shown on the left
506 and right, respectively.

507 **Figure 3 PT2385 disrupts subunit-subunit interactions in HIF-2 heterodimers.** **a**, Co-IP results showing
508 the destabilizing effect of PT2385 on the dimerization between overexpressed full-length HIF-2 α and
509 ARNT proteins. This experiment was independently repeated twice with similar results. **b-c**, Disrupting
510 effects of PT2385 on the heterodimerization of HIF-2 α -ARNT (**b**) and HIF-1 α -ARNT (**c**), as measured by
511 the TR-FRET-based assay. **d**, Interaction profile of ARNT and HIF-2 α mutant M252A. **e**, Disrupting effect
512 of PT2385 on the dimerization of ARNT and HIF-2 α mutant M252A. **f**, Comparison of PT2385's
513 inhibitory effects at 10 μ M on expression of HIF-2 target genes in HEK293T cells transfected with wild-
514 type HIF-2 α or M252A mutant. Error bars, mean \pm s.d.; n=3 (distinct replicates for cell cultures). Gels
515 for purified proteins and uncropped blots can be found in **Supplementary Fig. 13**.

516 **Figure 4 Newly identified antagonist T1001 points to a common inhibitory mechanism.** **a**, Chemical
517 structure of T1001. **b**, Binding of T1001 to the HIF-2 α PAS-B domain (K_d about 246 nM) measured by
518 MST. **c**, Inhibition on the expression of HIF-2 α target genes in 786-O cells by PT2385 (1 μ M) and T1001
519 (10 μ M). **d**, Binding site of T1001 within the HIF-2 α PAS-B pocket, with green meshes showing the $F_o -$
520 F_c omit map contoured at 3.0 σ . **e**, Comparison of T1001's inhibitory effects at 10 μ M on expression of
521 HIF-2 target genes in HEK293T cells transfected with wild-type HIF-2 α or M252A mutant. **f**, Comparison
522 of HIF-2 α residues surrounding antagonists in the PAS-B structures. The ligands and residues are in
523 magenta, pink and brown, for PT2385, OX3 and T1001 respectively. **g**, A mechanistic diagram showing
524 how antagonist binding leads to the movement of M252 to disrupt HIF-2 α -ARNT heterodimers. The
525 proximate positions of M252 side-chain in *apo* (orange) and antagonist-bound structures are compared
526 and related to the disruption potency. Error bars, mean \pm s.d.; n=3 (distinct replicates for cell cultures).

527 **Figure 5 The allosteric mechanism of agonist M1001.** **a**, Chemical structure of M1001. **b**, Binding of
528 M1001 to the HIF-2 α PAS-B domain (K_d about 667 nM) measured by MST. **c**, Opposite effects on the

529 expression of HIF-2 target genes in 786-O cells by PT2385 (1 μ M) and M1001 (10 μ M). **d**, Binding
530 position for M1001 (circled in black) within the entire HIF-2 α -ARNT crystal structure. The visible loop
531 region between ARNT PAS-A and PAS-B domains (A/B loop) is also indicated. **e**, Close-up look at the
532 location of M1001 inside the HIF-2 α PAS-B domain, with green meshes showing the $F_o - F_c$ omit map
533 contoured at 2.7σ . **f**, Interactions of M1001 (magenta) with surrounding residues in the pocket. **g**, The
534 overall arrangement of ARNT and HIF-2 α PAS-B domains is displayed in the middle, with the HIF-2 α
535 PAS-B domains from M1001-bound (cyan) or *apo* (orange) complexes superimposed; while enlarged or
536 rotated views on both sides show the conformational changes due to M1001 binding. The side-chain
537 movement of HIF-2 α Y281 not only promotes an additional hydrogen bond between HIF-2 α Y281 and
538 ARNT Y456 (right), but also altered the confirmation of HIF-2 α E287 and enabled its interaction with
539 ARNT N350 on the PAS-A/B loop (left). **h**, H/D-ex MS results mapped on the structure of HIF-2 α -ARNT
540 complex. The regions showing dynamic changes upon M1001 binding are colored according to the
541 maximum differences of deuteration levels (dark blue for -50 to -40%, pale purple for -40 to -25%, and
542 pink for 25 to 40%) as compared to the *apo* form complex (detailed in **Supplementary Fig. 11**), on top
543 of the background colors of HIF-2 α (gray) and ARNT (pale yellow). Enlarged and rotated views of dimer
544 interfaces between the two PAS-B domains, and between HIF-2 α PAS-A and PAS-B domains are shown
545 on the left and right, respectively. Error bars, mean \pm s.d.; n=3 (distinct replicates for cell cultures).

546 **Figure 6 The agonistic effects of M1002.** **a**, Chemical structure of M1002. **b**, Clear agonistic effects on
547 the expression of HIF-2 target genes in 786-O cells by M1002 (10 μ M) as compared with the antagonist
548 PT2385 (1 μ M). **c**, TR-FRET-based protein binding assays testing the effects of M1002 on the
549 associations between ARNT and its partners HIF-2 α , HIF-1 α and NPAS3, respectively. **d**, Comparison of
550 M1002's agonistic effects at 10 μ M on HIF-2 target genes in HEK293T cells transfected with wild-type

551 HIF-2 α or Y281A mutant. Error bars, mean \pm s.d.; n=3 (distinct replicates for cell cultures). **e**, Co-IP
552 results showing the effects of HIF-2 α ligands (PT2385, T1001, M1001 and M1002 at various
553 concentrations) on the association between full-length HIF-2 α and VHL proteins. This experiment was
554 independently repeated twice with similar results.

555

556 **ONLINE METHODS**

557 **Plasmid construction and site-directed mutagenesis.** Recombinant expression plasmids containing the
558 N-terminal bHLH-PAS-A-PAS-B regions of mouse HIF-2 α and ARNT proteins, pSJ2-HIF-2 α (3-361) and
559 pMKH-ARNT (82-464), as well as the full-length plasmids pCMV-Tag4-HIF-2 α (Flag-tagged) and pCMV-
560 Tag1-ARNT (Myc-tagged) used in co-immunoprecipitation, were described previously⁸. To express the
561 single PAS-B domain of HIF-2 α , its DNA segment coding for residues 241-361 was cloned into the pSJ2
562 vector. For the plasmid construction of GFP-tagged ARNT used in the TR-FRET assay, we cloned ARNT
563 DNA segment coding for residues 82-470, and amplified the DNA of Aequorea GFP from a pAdTrack-
564 CMV plasmid (gifted by Dr. Denny Liu at SBP). Two DNA segments were then further digested and
565 ligated using a BamHI cutting site designed at the C-terminus of ARNT and N-terminus of GFP, before
566 inserting together into the pMKH vector to produce a chimeric ARNT-GFP protein with no purification
567 tags. Site-directed mutagenesis was performed on corresponding wild-type HIF-2 α or ARNT plasmids
568 and confirmed by DNA sequencing.

569 **Protein expression and purification.** To obtain HIF-2 α -ARNT complex proteins, the pSJ2-HIF-2 α
570 plasmid was co-transformed along with pMKH-ARNT into BL21-CodonPlus (DE3)-RIL competent cells
571 (Agilent Technologies). Following 0.1 mM IPTG induced protein expression overnight at 16 °C, cell

572 pellets were lysed by sonication, and supernatants were applied onto pre-packed His-Bind resin
573 (Novagen). The bound proteins were further purified using SP Sepharose (GE Healthcare), and the
574 eluted fractions were then loaded on a HiLoad 16/60 Superdex 200pg gel filtration column (GE
575 Healthcare) equilibrated in 20 mM Tris (pH 8.0) and 400 mM NaCl. DTT was added to the pooled
576 protein peak fractions at 10 mM. The heterodimeric proteins of HIF-2 α and ARNT-GFP were prepared
577 similarly as described above, except that the pMKH-ARNT-GFP plasmid was used in the place of pMKH-
578 ARNT. The ARNT-GFP protein was co-expressed and purified in complex with HIF-1 α and NPAS3
579 (plasmids made in our previous studies^{3,8}), respectively. The single PAS-B domain of HIF-2 α was
580 produced by transformation of pSJ2-HIF-2 α (241-361) into BL21-CodonPlus (DE3)-RIL, followed by
581 overnight expression, and purification using His-tag affinity chromatography and gel filtration
582 chromatography.

583 **MST (microscale thermophoresis) binding assay.** The binding affinities of HIF-2 α ligands were
584 measured using MST method. Purified HIF-2 α protein (PAS-B domain) was labeled with the Monolith
585 NT™ Protein Labeling Kit RED. Compounds were diluted in a range of concentrations and mixed with
586 labeled protein at room temperature in the assay buffer containing 20 mM Tris (pH 7.5), 50 mM NaCl,
587 5 mM β -mercaptoethanol, 0.05% Tween-20 and 1% DMSO. Mixed samples were loaded into Monolith
588 TM standard-treated capillaries, and the thermophoresis was carried out on a Monolith NT.115
589 instrument (NanoTemper Technologies GmbH). Binding was measured with 20% LED power and
590 “medium” MST power, with an optimized time setting (5s Fluo, Before; 20s MST On; 5s Fluo, After). K_d
591 values were obtained by fitting the MST data in the GraphPad Prism 7 software.

592 **FP (fluorescence polarization) DNA binding assay.** The preparation of fluoresceinated double-strand
593 HRE DNA (6-FAM labeled F-strand: 5'-GGCTGCGTACGTGCGGGTCGT-3'; unlabeled R-strand: 5'-

594 ACGACCCGCACGTACGCAGCC-3') was described previously⁸. HIF-2 α -ARNT protein complex was diluted
595 in a 2-fold series in binding buffer (20 mM Tris pH 8.0, 20 mM NaCl), and each sample was incubated
596 with 0.1 μ M, 1 μ M or 10 μ M PT2385 (MedChemExpress HY-12867, 99.48% purity) for 1 hour (with the
597 same amount of 0.1% DMSO as a control), before binding assays started by the addition of 2 nM DNA.
598 The FP signals were recorded using black 96-well plates on a Synergy H1 microplate reader (BioTek
599 Instruments), and K_d values were calculated by fitting curves in GraphPad Prism 7.

600 **Luciferase reporter assay.** 786-O cells with a stable-transfected HRE-luc reporter were kindly provided
601 by Dr. Ian Pass at SBP. These cells were seeded in RPMI1640 medium with 10% FBS in 96-well plates at
602 5×10^4 per well, and one day later treated with PT2385 at different concentrations (final DMSO
603 concentration kept at 0.1%). After 24-hour incubation, cells were lysed and analyzed using Steady-Glo
604 Luciferase Assay System (Promega). To test the transcriptional activities of HIF-2 α harboring the
605 cancer-related mutations, HEK293T cells (ATCC CRL-3216) were seeded in 24-well plates in DMEM
606 containing 10% FBS, and one day later transfected with 200 ng of pCMV-Tag4-HIF-2 α (WT, mutants or
607 empty plasmid), 1 ng of pRL (control Renilla luciferase) and 100 ng of HRE-luc reporter using 0.6 μ L
608 jetPRIME reagent for each well. Medium was refreshed after overnight transfection, and luciferase
609 activity was measured another 24 hours later using the Dual-Glo Luciferase Assay System (Promega).
610 Final data were normalized by the relative ratio of firefly and Renilla luciferase activity.

611 **Real-time PCR.** 786-O cells (ATCC CRL-1932) were cultured in RPMI1640 medium with 10% FBS in 6-
612 well plates at 37°C in 5% CO₂. For the treatment, antagonists or agonists were added at various
613 concentrations with the equal amount of 0.1% DMSO as a control. After 24 hours, cells were collected,
614 and RNA was isolated with EZNA Total RNA Kit (Omega Bio-tek), followed by cDNA synthesis using
615 High-Capacity cDNA Reverse Transcription Kit (Thermo Fisher Scientific). HEK293T cells were seeded in

616 6-well plates and transfected with pCMV-Tag4-HIF-2 α plasmids (WT, mutants M252A or Y281A).
617 Medium was refreshed after overnight transfection, and cells were treated with 10 μ M compounds
618 (PT2385, T1001 or M1002) in 0.1% DMSO for 24 h before RNA isolation.

619 Hep3B cells (ATCC HB-8064) were cultured in DMEM medium with 10% FBS in 6-well plates. To
620 test the inhibitory effects of PT2385, cells were first placed overnight in normoxia (21% O₂) and
621 hypoxia (1% O₂) conditions, respectively. Then they were treated with 0.1% DMSO or 10 μ M PT2385
622 for 8 h before RNA isolation. For the co-treatment of PHD inhibitors and HIF-2 α agonist, Hep3B cells
623 were incubated with 10 μ M of molidustat (Cayman Chemical 15297) or roxadustat (Cayman Chemical
624 15294) for 8 h before 5 μ M of M1002 (Molport 001-006-026, >95% purity) was added into the medium
625 (final DMSO concentration all kept at 0.1%). After another 24 hours, cells were collected for RNA
626 isolation and cDNA synthesis.

627 Real-time PCR was performed on the StepOnePlus system using Fast SYBR Green Master Mix
628 (Thermo Fisher Scientific). The targeted gene expressions were normalized to the expression of Beta
629 Actin (*ACTB*) in the same sample. PCR primers were synthesized by Integrated DNA Technologies as
630 follows: *ACTB* (F: GCACAGAGCCTCGCCTT, R: GTTGTGACGACGAGCG); *VEGFA* (F:
631 TACCTCCACCATGCCAAGTG, R: ATGATTCTGCCCTCTCCTTC); *NDRG1* (F: CTCCTGCAAGAGTTTGATGTCC,
632 R: TCATGCCGATGTCATGGTAGG); *GLUT1* (F: TCTGGCATCAACGCTGTCTTC, R:
633 CGATACCGGAGCCAATGGT); *CyclinD1* (F: TGGAGCCCGTGAAAAAGAGC, R:
634 TCTCCTTCATCTTAGAGGCCAC); *EPO* (F: GGAGGCCGAGAATATCACGAC, R: CCCTGCCAGACTTCTACGG);
635 and *PGK1* (F: TTAAAGGGAAGCGGGTCGTTA, R: TCCATTGTCCAAGCAGAATTGA).

636 **Co-IP (immunoprecipitation).** Similar to our previous work⁸, HEK293T cells were seeded in 10 cm
637 dishes and cultured in DMEM containing 10% FBS at 37°C with 5% CO₂. One day later, cells were

transfected with 2 μ g pCMV-Tag4-HIF-2 α (wild-type or mutants) and 6 μ g pCMV-Tag1-ARNT (or pCMV-Tag1-VHL) plasmids by 16 μ L jetPRIME reagent (Polyplus-transfection). After overnight incubation, medium was refreshed with 50 μ M 2,2'-dipyridine and various concentrations of PT2385 (or other ligands) in 0.15% DMSO. Another 24 hours later, cells were harvested and sonicated in 700 μ L lysis buffer (1X TBS with 1 mM EDTA, 1% TRITON X-100 and 1X protease inhibitor cocktail). About 40 μ g of supernatant was saved as input for western blot using Monoclonal ANTI-FLAG M2 antibody (Sigma F1804) and anti-Myc rabbit mAb (Cell Signaling #2278). Immunoprecipitation was performed with 1 mg of supernatant and 40 μ L of ANTI-FLAG M2 affinity gel suspension (Sigma A2220), followed by western blot using the anti-Myc antibody.

Crystallization and X-ray data collection. HIF-2 α -ARNT protein complexes were crystallized by mixing equal volume of protein and the reservoir containing tacsimate (pH 7.0) and PEG3350 using sitting-drop vapor diffusion method at 16 $^{\circ}$ C as before⁸. For PT2385 and M1001 (MolPort 001-008-374, >95% purity), crystals of HIF-2 α -ARNT in complex with ligands were obtained by adding compounds (100 μ M) to the drops containing *apo* protein crystals and soaking overnight before crystal harvest. For T1001 (Santa Cruz Biotechnology sc-201431, \geq 98% purity), co-crystallization of HIF-2 α -ARNT with ligands (100 μ M) was successful. 30% PEG400 was added into the reservoir solution to cryoprotect the crystals before flash frozen. Diffraction data were collected at 100 K at the Argonne National Laboratory SBC-CAT 19ID beamline, and processed using the HKL3000 program⁴³.

Structure determination and refinement. The structures of HIF-2 α -ARNT in complex with ligands were solved by molecular replacement with the program Phaser⁴⁴, using the *apo* HIF-2 α -ARNT structure (PDB code 4ZP4) as the search model. Further manual model building was facilitated using Coot⁴⁵, combined with the structure refinement using phenix.refine⁴⁶. The diffraction data and final statistics

are summarized in **Supplementary Table 1**. The Ramachandran statistics, as calculated by Molprobity⁴⁷, are 92%/0, 93%/0.2% and 93%/0.2% (favored/outliers) for complex structures of HIF-2 α -ARNT-PT2385, HIF-2 α -ARNT-T1001 and HIF-2 α -ARNT-M1001, respectively. All the structural figures were prepared using PyMol (The PyMol Molecular Graphics System, Version 1.3, Schrödinger, LLC).

H/D-ex MS (hydrogen-deuterium exchange mass spectrometry) assay. Hydrogen-deuterium exchange experiments were performed using the in-house deuterium exchange system^{48,49}. In this system, the enzymatic digestion, peptide separation and MS analysis are all fully automated. To start the H/D-ex reaction, 3 μ l pre-chilled protein stock solution at 19.5 μ M (free HIF-2 protein complex, HIF-2 protein complex combined with agonists or antagonists) was diluted into 9 μ l D₂O buffer (8.3 mM Tris, 250 mM NaCl, in D₂O, pD_{READ} 7.2), and incubated at 0 °C for 30, 100, 300, 1000, 3000 and 10000 s, respectively. At indicated times, 18 μ l cold acidic buffer (1.6 M GuHCl, 100 mM Glycine, 16.6% (v/v) Glycerol, pH 2.4) was added to quench the exchange reaction. To maximize sequence coverage of HIF2 α -ARNT complex, various concentrations of GuHCl (0.08, 0.8, 1.6 and 3.2 M) were used to optimize quench condition, and the best coverage map was obtained using 1.6 M GuHCl quench buffer. Quenched samples were then frozen on dry ice and were passed through an immobilized pepsin column (16 μ l bed volume) on ice in H₂O containing 0.05% (v/v) trifluoroacetic acid at 20 μ l min⁻¹ for pepsin digestion. The pepsin column was made by conjugating pepsin onto POROS 20 AL self-pack aldehyde-activated resin at 40 mg/ml via couple chemistry and packing at 5 ml min⁻¹ into one 1x20 mm guard column. The proteolytic products were processed on a C18 trap column for desalting (Optimizetechnologies, Magic C18 AQ, 0.2x2 mm) and on a Michrom Magic C18 (3 μ m, 0.2x50 mm, 200 Å) with a 30-min linear acetonitrile gradient (6.4-38.4%) for separation. The eluted samples were subjected to an OrbiTrap Elite mass spectrometer (Thermo Fisher Scientific), which was optimized for H/D-ex analysis as previously

682 reported⁵⁰. The identification of peptides was performed using Proteome Discoverer (Thermo Fisher
683 Scientific), and their deuteration levels were determined by HDEXaminer (Sierra Analytics Inc). In
684 addition, H/D-ex analysis was also conducted on both non-deuterated and fully deuterated samples to
685 correct the back-exchange⁵¹. The Peptide coverage map for HIF-2 α -ARNT is shown in **Supplementary**
686 **Fig. 14**.

687 **TR-FRET (time-resolved fluorescence energy transfer)-based *in vitro* binding assay.** This method was
688 developed based on the LanthaScreen technology (Thermo Fisher Scientific). Purified protein
689 complexes of GFP-tagged ARNT and His-tagged HIF-2 α , HIF-1 α or NPAS3 were dispensed into 1536-well
690 plates with serial dilution, in the assay buffer containing 20 mM Tris (pH 7.4), 100 mM NaCl, 1mM DTT
691 and 0.005% tween-20. After addition of the LanthaScreen Elite Terbium-labeled anti-His antibody
692 (Thermo Fisher Scientific PV5863) into each well at 5 nM, the plate was centrifuged at 800 rpm for 1
693 min and kept in dark for 1 h. Then the protein interactions were monitored via the energy transfer
694 signal with an EnVision multilabel plate reader (PerkinElmer). The TR-FRET value was determined as a
695 ratio of the signal measured at 520 nm (GFP) to the signal measured at 492 nm (terbium). The
696 apparent K_d values of each protein complex were calculated by plotting the ratios (520 nm/492 nm)
697 against the protein concentrations in GraphPad Prism 7. To test effects of antagonists or agonists on
698 heterodimerization, similar protocols were used except that the protein concentration was kept at 50
699 nM, while the compounds were added in a wide range of serial dilution with 1% DMSO.

700 **Thermal shift binding assays.** The initial screening based on thermal shift method was carried out in
701 384-well plates with a LightCycler 480 instrument (Roche). The concentrations for protein and
702 compounds used in the screening were 2 μ M and 20 μ M (with 0.1% DMSO), respectively. To get
703 quantitative thermal shift (ΔT_m) values, we ran this assay in 96-well format using the Protein Thermal

704 Shift (PTS) Dye Kit on a StepOnePlus qPCR machine (Thermo Fisher Scientific), according to the
705 manufacturer's instructions. For each well, the concentration of protein complex was about 1.5 μ M,
706 and all the antagonists or agonists were tested at 10 μ M in the assay buffer containing 20 mM Tris (pH
707 8.0), 400 mM NaCl and 0.1% DMSO. Final data were analyzed using the PTS software v1.2 to calculate
708 the Derivative curve determined T_m values and to compare ΔT_m values of different ligands.

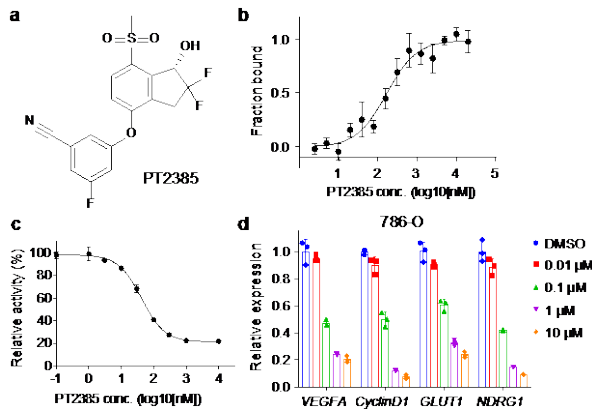
709 **AS-MS (affinity selection-mass spectrometry) screening.** We employed a 32,000-chemical library
710 consisting of 80 distinct pools of 400 compound mixtures, to rapidly identify the preferential binding of
711 candidate molecules to our protein targets. Diluted HIF-2 α -ARNT protein was dispensed into wells with
712 a final protein concentration of 10 μ M and a final compound concentration of 2 μ M each in about 1.5%
713 DMSO. The plate was kept in a shaker at room temperature for 1 h with gentle mixing, to allow fully
714 interactions between protein and compounds. After spinning the plate at 1500 g for 1 min to
715 precipitate the insoluble components, supernatant from each well was subjected to a size exclusion
716 PolyHYDROXYETHYL A column (PolyLC Inc.) to separate the protein-compound complexes and unbound
717 components. Isolated protein-compound complexes were then passed into a reversed phase Accucore
718 C18 LC column (Thermo Fisher Scientific) in a heat chamber. Heat-released compounds were further
719 separated and analyzed by TOF-MS system (Agilent Technologies). The key parameters of above two
720 screens (PTS and AS-MS) are summarized in **Supplementary Table 2**.

721 **Data availability.** The three sets of structural data from HIF-2 α -ARNT crystals in complex with PT2385,
722 T1001 and M1001 are available in wwPDB under accession codes 6E3S, 6E3T and 6E3U, respectively.
723 Other data shown in the article are available from the correspond authors upon reasonable request.

724 **References**

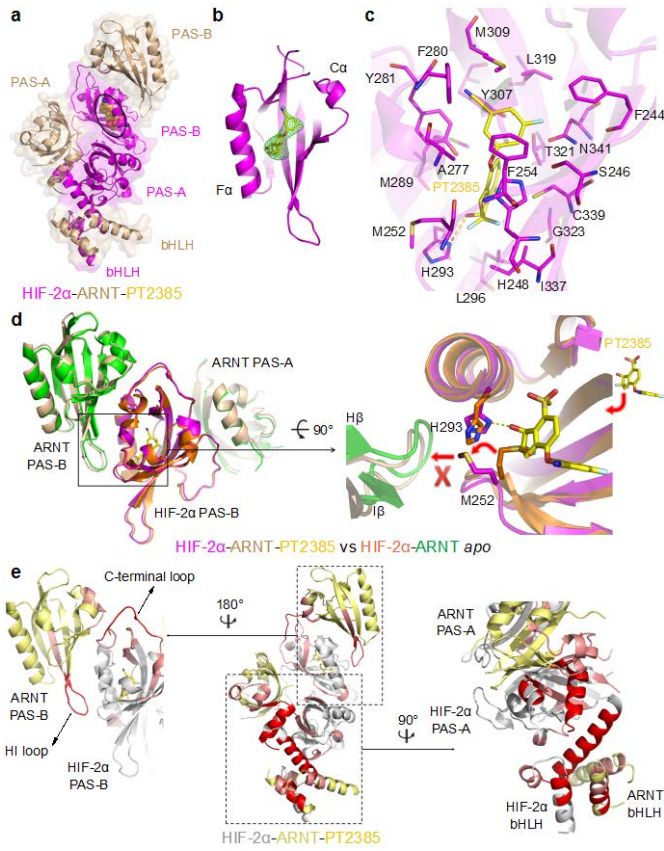
- 725 43. Minor, W., Cymborowski, M., Otwinowski, Z. & Chruszcz, M. HKL-3000: the integration of data
726 reduction and structure solution--from diffraction images to an initial model in minutes. *Acta*
727 *Crystallogr D Biol Crystallogr* **62**, 859-66 (2006).
- 728 44. McCoy, A.J. et al. Phaser crystallographic software. *J Appl Crystallogr* **40**, 658-674 (2007).
- 729 45. Emsley, P., Lohkamp, B., Scott, W.G. & Cowtan, K. Features and development of Coot. *Acta*
730 *Crystallogr D Biol Crystallogr* **66**, 486-501 (2010).
- 731 46. Adams, P.D. et al. PHENIX: a comprehensive Python-based system for macromolecular structure
732 solution. *Acta Crystallogr D Biol Crystallogr* **66**, 213-21 (2010).
- 733 47. Chen, V.B. et al. MolProbity: all-atom structure validation for macromolecular crystallography.
734 *Acta Crystallogr D Biol Crystallogr* **66**, 12-21 (2010).
- 735 48. Marsh, J.J. et al. Structural insights into fibrinogen dynamics using amide hydrogen/deuterium
736 exchange mass spectrometry. *Biochemistry* **52**, 5491-502 (2013).
- 737 49. Woods, V.L., Jr. & Hamuro, Y. High resolution, high-throughput amide deuterium exchange-
738 mass spectrometry (DXMS) determination of protein binding site structure and dynamics: utility
739 in pharmaceutical design. *J Cell Biochem Suppl Suppl* **37**, 89-98 (2001).
- 740 50. Walters, B.T., Ricciuti, A., Mayne, L. & Englander, S.W. Minimizing back exchange in the
741 hydrogen exchange-mass spectrometry experiment. *J Am Soc Mass Spectrom* **23**, 2132-9
742 (2012).
- 743 51. Li, S. et al. Mechanism of intracellular cAMP sensor Epac2 activation: cAMP-induced
744 conformational changes identified by amide hydrogen/deuterium exchange mass spectrometry
745 (DXMS). *J Biol Chem* **286**, 17889-97 (2011).
- 746

747



748

749 Figure 1



750

751 Figure 2

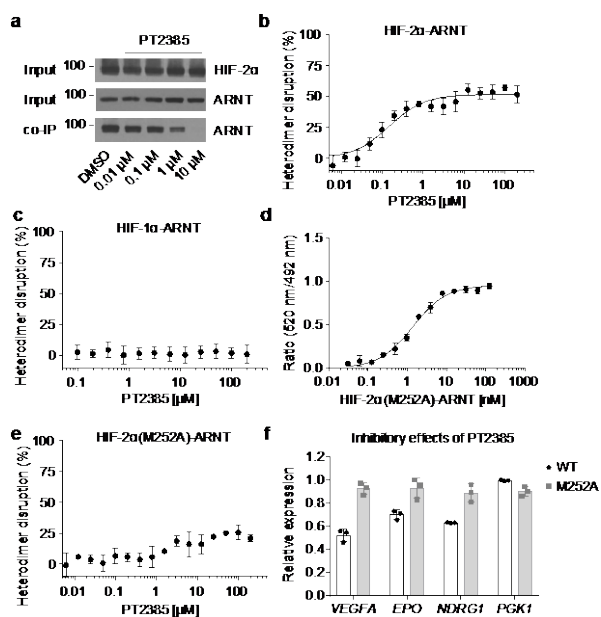


Figure 3

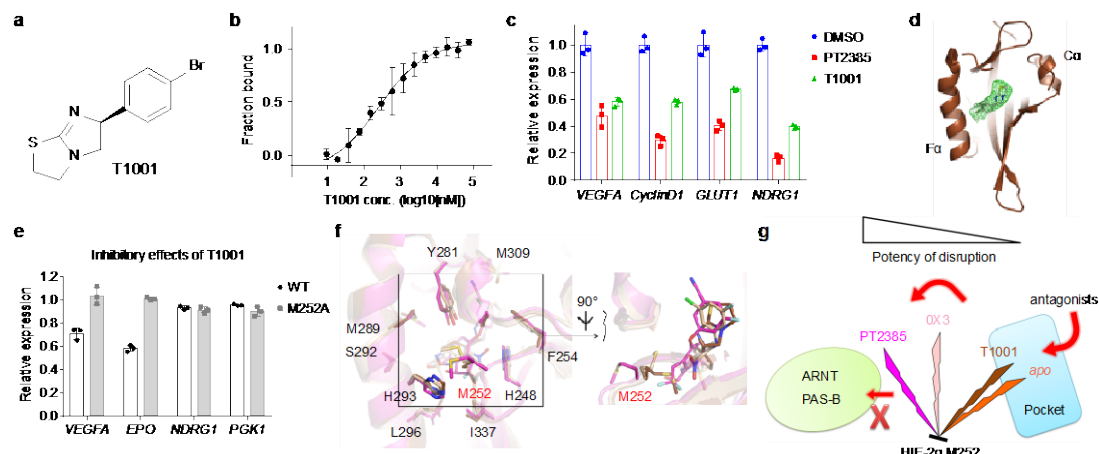


Figure 4

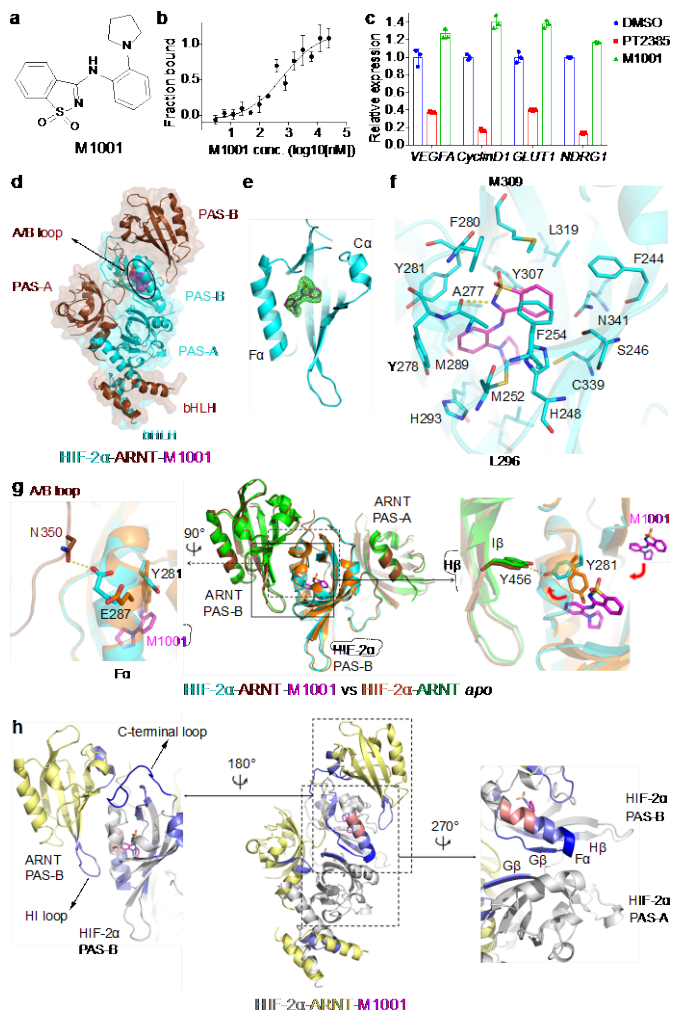


Figure 5

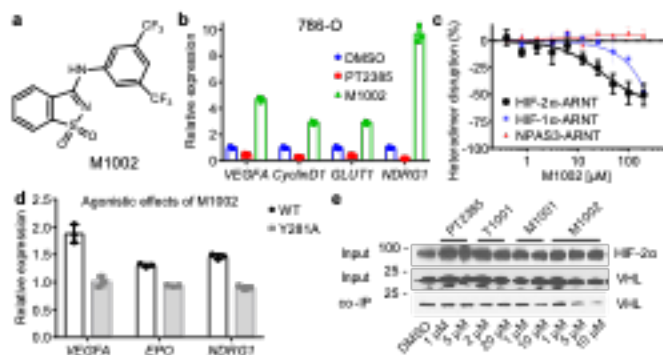


Figure 6

Supplementary Table 1 Data collection and refinement statistics

	HIF-2 α -ARNT- PT2385	HIF-2 α -ARNT- T1001	HIF-2 α -ARNT- M1001
PDB ID	6E3S	6E3T	6E3U
Data collection			
Space group	P 21	P 21	P 21
Cell dimensions			
<i>a</i> , <i>b</i> , <i>c</i> (Å)	49.01, 97.90, 77.97	49.03, 97.98, 77.43	48.95, 98.85, 77.08
α , β , γ (°)	90, 107.43, 90	90, 107.10, 90	90, 107.20, 90
Resolution (Å)	50.0-2.90 (2.95- 2.90) *	50.0-2.96 (3.01- 2.96)	50.0-2.85 (2.90- 2.85)
<i>R</i> _{merge}	9.9 (76.5)	7.5 (80.3)	9.3 (74.1)
<i>I</i> / σ <i>I</i>	11.4 (1.1)	18.7 (1.1)	15.3 (1.7)
Completeness (%)	98.7 (92.8)	94.3 (71.1)	98.0 (97.7)
Redundancy	2.6 (2.2)	4.9 (4.2)	4.6 (4.2)
Refinement			
Resolution (Å)	49.0-3.00 (3.11- 3.00)	37.0-3.00 (3.11- 3.00)	35.1-2.85 (2.95- 2.85)
No. reflections	14027 (1393)	13418 (1179)	16104 (1566)
<i>R</i> _{work} / <i>R</i> _{free}	21.3/25.1 (27.5/33.3)	25.0/30.8 (33.3/36.3)	19.9/25.8 (27.5/31.6)
No. atoms			
Protein	4366	4251	4432
Ligand/ion	26	15	23
<i>B</i> -factors			
Protein	115.9	114.1	85.7
Ligand/ion	103.8	132.5	63.4
R.m.s. deviations			
Bond lengths (Å)	0.010	0.011	0.011
Bond angles (°)	1.28	1.45	1.38

One crystal was used for each structure.

*Values in parentheses are for the highest-resolution shell.